Contrib Mineral Petrol (2013) 166:423–434
DOI 10.1007/s00410-013-0883-4

ORIGINAL PAPER

Quantification of the ferric/ferrous iron ratio in silicates by scanning transmission X-ray microscopy at the Fe $L_{2,3}$ edges

Franck Bourdelle · Karim Benzerara ·
Olivier Beyssac · Julie Cosmidis · Daniel R. Neuville ·
Gordon E. Brown Jr. · Erwan Paineau

Received: 15 February 2013 / Accepted: 29 April 2013 / Published online: 4 June 2013

Abstract Estimation of $Fe^{3+}/\Sigma Fe$ ratios in materials at the submicrometre scale has been a long-standing challenge in the Earth and environmental sciences because of the usefulness of this ratio in estimating redox conditions as well as for geothermometry. To date, few quantitative methods with submicrometric resolution have been developed for this purpose, and most of them have used electron energy-loss spectroscopy carried out in the ultra-high vacuum environment of a transmission electron microscope (TEM). Scanning transmission X-ray microscopy (STXM) is a relatively new technique complementary to TEM and is increasingly being used in the Earth sciences. Here, we detail an analytical procedure to quantify the $Fe^{3+}/\Sigma Fe$ ratio in silicates using Fe $L_{2,3}$-edge X-ray absorption near edge structure (XANES) spectra obtained by STXM, and we discuss its advantages and limitations. Two different methods for retrieving $Fe^{3+}/\Sigma Fe$ ratios from XANES spectra are calibrated using reference samples with known Fe^{3+} content by independent approaches. The first method uses the intensity ratio of the two major peaks at the L_3-edge. This method allows mapping of $Fe^{3+}/\Sigma Fe$ ratios at a spatial scale better than 50 nm by the acquisition of 5 images only. The second method employs a 2-eV-wide integration window centred on the L_2 maximum for Fe^{3+}, which is compared to the total integral intensity of the Fe L_2-edge. These two approaches are applied to metapelites from the Glarus massif (Switzerland), containing micrometre-sized chlorite and illite grains and prepared as ultrathin foils by focused ion beam milling. Nanometre-scale mapping of iron redox in these samples is presented and shows evidence of compositional zonation. The existence of such zonation has crucial implications for geothermometry and illustrates the importance of being able to measure $Fe^{3+}/\Sigma Fe$ ratios at the submicrometre scale in geological samples.

Communicated by J. Hoefs.

F. Bourdelle · K. Benzerara · O. Beyssac · J. Cosmidis
IMPMC, UPMC-CNRS, Case courrier 115, 4 Place Jussieu,
75252 Paris cedex 05, France
e-mail: Karim.Benzerara@impmc.upmc.fr

F. Bourdelle (✉)
GeoRessources, Université de Lorraine, UMR 7359 CNRS,
54506 Vandœuvre-lés-Nancy, France
e-mail: franck.bourdelle@gmail.com

D. R. Neuville
Géochimie et Cosmochimie, Institut de Physique du Globe de
Paris, Université Paris Diderot, Sorbonne Paris Cité, UMR 7154
CNRS, 1 rue Jussieu, 75005 Paris, France

G. E. Brown Jr.
Surface and Aqueous Geochemistry Group, Department of
Geological and Environmental Sciences, Stanford University,
Stanford, CA 94305-2115, USA

G. E. Brown Jr.
SLAC Natl Accelerator Lab, Stanford Synchrotron Radiation
Lightsource, Menlo Pk, CA 94025, USA

E. Paineau
Laboratoire de Physique des Solides, Université Paris-Sud, UMR
8502 CNRS, Bâtiment 510, 91405 Orsay cedex, France

E. Paineau
Laboratoire Interdisciplinaire sur l'Organisation Nanométrique
et Supramoléculaire, CEA Saclay, IRAMIS,
91191 Gif-sur-Yvette cedex, France

Keywords Ferric/ferrous iron · STXM · XANES spectroscopy · $L_{2,3}$-edge · Redox mapping · Silicate

Introduction

Determination of the redox state of iron and its spatial variations in sediments and rocks is of critical importance in both geosciences and environmental sciences, because of the need to understand redox state during their deposition or formation as well as subsequent changes in redox state due to weathering and other processes (e.g., de Andrade et al. 2006; Muñoz et al. 2006; Bernard et al. 2010; Benzerara et al. 2011a; Bolfan-Casanova et al. 2012; Stagno et al. 2013). In addition, quantification of $Fe^{3+}/\Sigma Fe$ ratios can yield a better insight into the chemistry of complex geological materials (e.g., Muñoz et al. 2006), or a better estimation of *P*–*T* conditions by geothermobarometers, when variations of the Fe^{3+} content within the crystals are taken into account (e.g., Schmid et al. 2003; de Andrade et al. 2006; Bourdelle et al. 2013a). Therefore, assessment of the $Fe^{3+}/\Sigma Fe$ ratio in minerals is an important and long-standing issue. Different techniques have been used extensively in the past for this purpose, including electron microprobe analysis (EMPA, e.g., Fialin et al. 2004), Mössbauer spectroscopy (e.g., Beaufort et al. 1992) X-ray photoelectron spectroscopy (XPS, e.g., Raeburn et al. 1997a, b) or X-ray absorption near edge structure (XANES) spectroscopy at the K edge (e.g., Waychunas et al. 1983; Bajt et al. 1994; Wilke et al. 2001, 2009; Berry et al. 2003, 2010). However, none of these methods provides spatial resolution at the few nanometres scale, which is particularly useful for studying chemical zonation patterns observed in low-temperature systems. Several studies (e.g., van Aken and Liebscher 2002) have shown that electron energy-loss spectroscopy (EELS) carried out in a transmission electron microscope (TEM) is a powerful method for determining the redox state of iron at a sub-micrometre resolution. However, it sometimes induces severe beam damage effects, such as electron beam-induced oxidation of iron (Lauterbach et al. 2000; Garvie et al. 2004), the effect of which can be corrected by measuring the signal as a function of time. Alternatively, XANES spectroscopy at the Fe $L_{2,3}$ edges carried out with a scanning transmission X-ray microscope (STXM) has been increasingly used in the Earth and environmental sciences to infer qualitatively $Fe^{3+}/\Sigma Fe$ ratios in geological and environmental samples at a spatial resolution of ~50 nm (e.g., Wasinger et al. 2003; Carlut et al. 2010; Lam et al. 2010; de Groot et al. 2010; Miot et al. 2011; Boulard et al. 2012). This technique has several advantages such as offering a high energy resolution (better than 0.1 eV at existing synchrotron facilities) and the possibility of maintaining samples under anoxic conditions before and during the measurement (e.g., Miot et al. 2009). However, no calibration of the STXM-based Fe $L_{2,3}$-edge XANES approach has yet been carried out, whereas calibration of the EELS approach was quantified by van Aken and Liebscher (2002). Fe $L_{2,3}$-edges result from $2p \rightarrow 3d$ electronic transitions, as shown by Wasinger et al. (2003). These authors described in detail the physical basis of Fe L edges and showed that information about iron valency can be retrieved from XANES spectra by a multiplet calculation approach (e.g., van der Laan and Kirkman 1992; Cressey et al. 1993). This approach is difficult to apply when dealing with mineral phases for which we do not know the structure. Alternatively, fitting of XANES spectra with a linear combination of normalised reference spectra has been performed by Miot et al. (2009), but requires appropriate Fe^{2+} and Fe^{3+} end-member reference compounds with Fe in the same local coordination environment as in the sample of interest. Van Aken and Liebscher (2002) have shown the possibility of a third approach that they calibrated for EELS and which uses an empirical correlation between $Fe^{3+}/\Sigma Fe$ ratios and a parameter (i.e., modified integral white-line intensity ratio) which is directly retrieved from EELS spectra at the Fe $L_{2,3}$ edges and is independent of the coordination environment of Fe to a first-order approximation.

Here, we propose an empirical approach similar to that of van Aken and Liebscher (2002) to calibrate the correlation between $Fe^{3+}/\Sigma Fe$ ratio and some parameters extracted from the STXM-derived XANES Fe $L_{2,3}$-edge spectra of reference silicate glasses and phyllosilicates. Two empirical calibrations are proposed, both of which offer a compromise between speed and accuracy of the analytical measurement. An application of this approach to ultra-thin sections of natural chlorites and micas is presented to illustrate the methodology and to further assess the range of applicability of these calibrations for STXM.

Materials and methods

Reference samples

The samples used in this study were reference synthetic silicate glasses, natural phyllosilicates and fayalite, prepared as powders or ultra-thin sections cut by focused ion beam (FIB) milling. The bulk chemical compositions of the five synthetic glasses were previously determined by Magnien et al. (2004). All samples are composed of similar proportions of Si, Mg, Ca, Na and Fe. The SiO_2 and FeO contents are ~52 and ~13 wt%, respectively. Bulk $Fe^{3+}/\Sigma Fe$ ratios were determined by wet chemistry, Mössbauer spectroscopy and EMPA and range from 0.09 to 0.94

Table 1 Reference samples used for XANES—Fe^{3+}/ΣFe ratio quantification

Type	Sample	Source	FeO wt%[a]	Fe^{3+}/ΣFe Redox ratio	Position of maximum peak intensity (eV)			
					L$_3$-a	L$_3$-b	L$_2$-a	L$_2$-b
Silicate glass	PyrNa	Magnien et al. (2004)	12.83	0.73 ± 0.03	708.57	710.04	721.68	723.54
Silicate glass	PyrNa17R	Magnien et al. (2004)	12.75	0.09 ± 0.01	708.36	710.77	721.37	723.54
Silicate glass	PyrNa5R	Magnien et al. (2004)	12.92	0.61 ± 0.01	708.57	710.04	721.68	723.54
Silicate glass	PyrNa750	Magnien et al. (2004)	12.68	0.94 ± 0.03	708.67	710.25	721.68	723.54
Silicate glass	PyrNa1200	Magnien et al. (2004)	13.52	0.89 ± 0.05	708.67	708.93	721.84	724.54
Nesosilicate	Fayalite	Neuville D. R.	70.50	0.00 ± 0.00[c]	708.09	710.71	720.75	723.54
Phyllosilicate	Smectite Nau-2	Keeling et al. (2000)	34.10	1.00 ± 0.00[c]	708.57	710.35	721.84	723.54
Phyllosilicate	Clintonite	Joswig et al. (1986)	3.01	0.69 ± 0.03[c]	708.25	710.08	721.49	723.53
Phyllosilicate	Ti-mica	Shingaro et al. (2005)	19.38	0.03 ± 0.03[c]	708.04	710.04	721.00	723.54
Phyllosilicate	Chlorite “Prochlorite”	MNHN[b]	14.50	0.30 ± 0.10[c]	708.26	710.21	721.51	723.51
Phyllosilicate	Chlorite Ch1	This study	40.10	0.17 ± 0.05	708.04	710.19	721.00	723.54
Phyllosilicate	Chlorite GAB 42	Rigault (2010)	28.50	0.14 ± 0.03	708.15	710.46	720.75	723.54
Phyllosilicate	Chlorite VNI 92	Rigault (2010)	20.73	0.35 ± 0.03	708.15	710.25	720.75	723.54
Phyllosilicate	Chlorite VNI 114	Rigault (2010)	20.82	0.20 ± 0.03	708.04	710.25	720.75	723.54

[a] ΣOxides wt% = 100 as basis and all iron reported as ferrous. [b] MNHN: Collection of Muséum National d'Histoire Naturelle, France. [c] assumed error deviation

(Table 1; Magnien et al. 2004). For STXM-XANES analyses, we ground these samples in deaerated and deionised water, inside an anoxic glove box (p(O$_2$) <50 ppm) to avoid oxidation during sample preparation.

The phyllosilicate samples have 2:1 and 2:1:1 structures, and their bulk compositions were investigated previously by Joswig et al. (1986); Keeling et al. (2000); Shingaro et al. (2005); Rigault (2010) and in the present study by EMP analyses. Total Fe contents vary significantly between samples and bulk Fe^{3+}/ΣFe ratios ranging between 0.03 and 1.0 were measured by Mössbauer spectroscopy, EXAFS (extended X-ray absorption fine structure) and/or EELS (Table 1). In addition, a fayalite sample was used as a pure Fe^{2+} reference. For STXM-XANES analyses, some samples (smectite Nau-2, chlorites GAB 42, VNI 92, VNI 114, fayalite) were prepared by grinding in deaerated and deionised water in an anoxic glove box (p(O$_2$) <50 ppm). Other samples (clintonite, chlorite “prochlorite”, chlorite Ch1, Ti-mica) were prepared by FIB milling.

Samples transparent to soft X-rays are needed to measure XANES spectra in the transmission mode of STXM, therefore requiring the preparation of thin samples. FIB foils were cut with a FEI Model 200 TEM FIB system at University Aix-Marseille using the protocol detailed by Heaney et al. (2001). A 30 kV Ga$^+$ beam operating at ~20 nA excavated the sample to a depth of 5 μm. The sample foil was then further thinned to ~80–100 nm at lower beam voltage (5 kV) and current (~ 100 pA), in order to remove the layer damaged by high-energy ions (Bourdelle et al. 2012).

Glarus field samples

The Glarus Alps (Switzerland) belongs to the Helvetic zone of the northern margin of the Central Alps and was affected by low-grade metamorphism. Details about the location and composition of the samples analysed by STXM in the present study are provided in Lahfid et al. (2010). The selected rock samples are metapelites, more or less clayey or sandy marls, with various proportions of quartz, calcite and clay minerals. Three samples (noted Glarus GL07 13, 16 and 20, as in Lahfid et al. 2010), containing chlorites and K-deficient micas, were milled by FIB. The compositions of the chlorites and micas were obtained on the FIB foils by analytical electron microscopy analyses described elsewhere (Bourdelle et al. 2012).

XANES spectroscopy

Part of the STXM analyses were performed at the advanced light source (ALS) (Lawrence Berkeley National Laboratory) on branch line 11.0.2.2 following the procedures described in Miot et al. (2009). The ALS storage ring was operated at 1.9 GeV and 500 mA current in a top-up mode. More details on the branch line 11.0.2.2 and beam characteristics are given by Bluhm et al. (2006). Stacks of images were obtained by scanning the sample in the x–y directions of selected sample areas over the 690–730 eV energy range (Fe $L_{2,3}$-edge) using an energy increment of 0.789 eV between 690 and 705 eV, 0.10 eV in the 705–713 eV energy range, 0.19 eV in the 713–719 eV energy range, 0.155 eV in the 719–726 eV energy range and 0.475 eV in the 726–730 eV energy range. The dwell time per pixel and energy point was 1.3 ms.

Some data (chlorite Ch1, chlorite "prochlorite" and Ti-mica) were acquired on the Pollux beamline at the Swiss Light Source (SLS, Villigen, Switzerland). The SLS synchrotron storage ring was operated at 2.4 GeV and 300 mA current in a top-up mode during data collection, and the characteristics of the beamline are detailed by Raabe et al. (2008). Stacks were obtained over the 690–730 eV energy range (Fe $L_{2,3}$-edge) using an energy increment of 0.667 eV between 690 and 700 eV, 0.15 eV in the 700–715 eV energy range, 0.40 eV in the 715–727 eV energy ranges and 0.89 eV in the 727–730 eV energy range. The dwell time per pixel and energy point was 3.5 ms.

At both the ALS and the SLS, focus was achieved systematically for each sample, and precision in the determination of the focus position was better than the focus depth. Image stacks were aligned, and XANES spectra were derived from areas of interest using the aXis2000 software (Hitchcock 2012). Potential beam damage caused by the incident photon beam was assessed by monitoring spectral changes at the Fe $L_{2,3}$-edge with increasing dwell times up to a hundred milliseconds (10, 50 and 100 ms).

Spectra processing

Energy calibration was performed using the gaseous neon $1s \rightarrow 3p$ electronic transition at 867.3 eV. As explained in Fig. 1, the processing of spectra consisted of two steps. First, the contribution of lower energy absorption edges (i.e., background) was removed so that in the end, the pre-edge region is set to 0 optical density (noted OD) with a slope of zero. For that purpose, a "linear background" correction was applied to the spectrum. Second, the two edge steps resulting from transitions to unoccupied states in the continuum were subtracted using the following double arctan function (Chen et al. 1995; van Aken and Liebscher 2002; Brotton et al. 2007):

$$f(\Delta E) = \frac{h_1}{\pi}\left(\arctan\left[\frac{\pi}{w_1}(\Delta E - E_1)\right] + \frac{\pi}{2}\right) + \frac{h_2}{\pi}\left(\arctan\left[\frac{\pi}{w_2}(\Delta E - E_2)\right] + \frac{\pi}{2}\right) \qquad (1)$$

where h_1 and h_2 are the step heights of the two arctan functions, w_1 and w_2 are fixed peak widths and E_1 and E_2 are the positions of the inflection points resulting in an energy near the edge onset. Here, w_1 and w_2 are fixed to

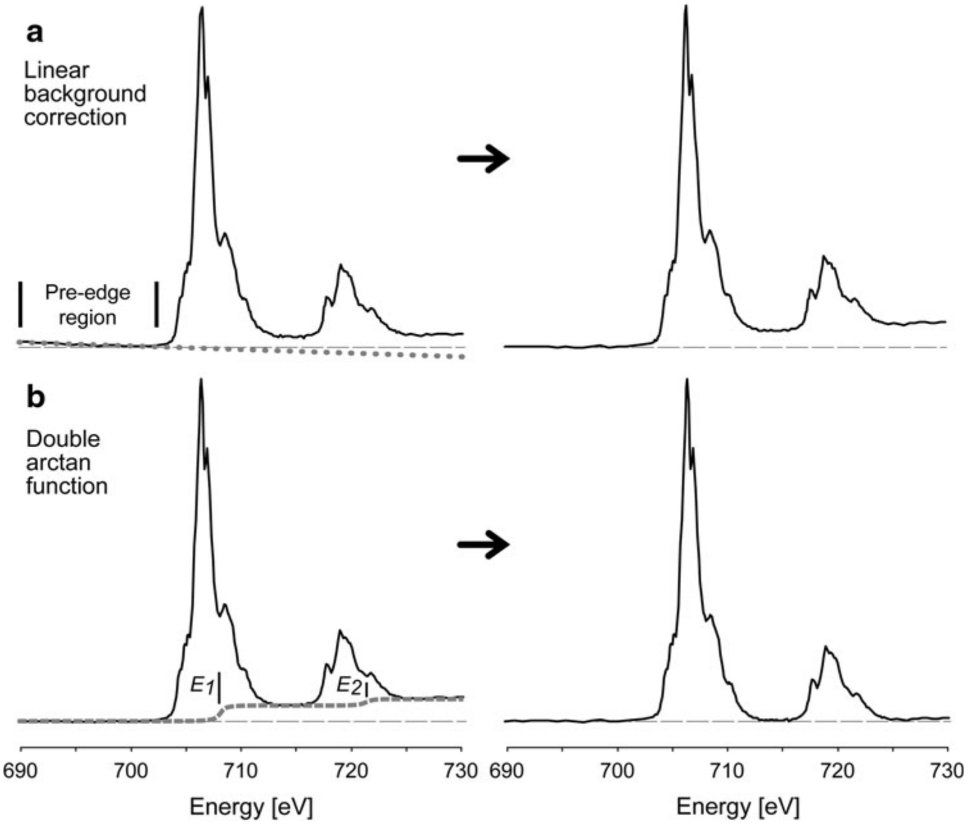

Fig. 1 Subtraction of background from XANES spectra at Fe L-edge, using linear (**a**) and double arctan (**b**) functions ($w_1 = w_2 = 1$ eV), for chlorite GAB 42

1 eV (Fig. 1). Brotton et al. (2007) proposed setting the function slope *w* at 5 eV, to account for the slow onset of the continuum. They argued that a value smaller than 5 eV could induce spurious structures in the background-corrected spectrum. We observed that values of $w = 1$ eV or $w = 5$ eV provided similar results.

Results and discussion

Evolution of Fe $L_{2,3}$-edge XANES spectra with changes in $Fe^{3+}/\Sigma Fe$

X-ray absorption near edge structure spectra at the Fe $L_{2,3}$-edges of the reference phyllosilicates, fayalite and five Fe-bearing silicate glasses, corrected for continuum absorption, are shown in Fig. 2, and the positions of major peaks are summarised in Table 1. These spectra are qualitatively similar to those described in several previous studies and were obtained using different analytical techniques (e.g., Crocombette et al. 1995; Heijboer et al. 2003; van Aken and Liebscher 2002). Four major Fe $L_{2,3}$-edge XANES peaks are present in all samples. The two major peaks on the L_3 edge are noted as "L_3-a" and "L_3-b", and similarly, the major peaks on the L_2 edge are noted as "L_2-a" and "L_2-b". For all samples examined, the measured separations of the Fe L_3 and L_2 maxima, due to spin–orbit splitting (van Aken and Liebscher 2002), are 12.9 ± 0.4 eV and 14.2 ± 1.4 eV for peaks a and b, respectively, in agreement with previous EELS and XANES studies (e.g., de Smit et al. 2008; de Groot et al. 2010). However, although most of the spectra show a single asymmetrical L_3-a peak, some of them (i.e., VNI 92, VNI 114 and GAB 42, fayalite) display an "L_3-a" split into two peaks. In addition, these specific spectra show additional peaks on the L_3-a side at ~706.3 and ~706.8 eV. According to Wasinger et al. (2003), the presence of these minor peaks may be due to a specific atomic environment and/or orbital co-valency of iron in these mineral phases. Similarly, several minor peaks can be observed at around 719.8 eV on the L_2-edge for several samples (VNI 92, VNI 114, GAB 42, PyrNa 17R, fayalite).

The relative intensities of the different major peaks vary depending on the $Fe^{3+}/\Sigma Fe$ ratio (Fig. 2). With increasing $Fe^{3+}/\Sigma Fe$ ratios, the relative intensity of the L_3-a peak decreases compared to that of the L_3-b peak; L_3-a is more intense than L_3-b in the XANES spectrum of the VNI 92 sample ($Fe^{3+}/\Sigma Fe = 0.35$), whereas the opposite is observed for PyrNa 5R ($Fe^{3+}/\Sigma Fe = 0.61$). Likewise, the relative intensity of L_2-a progressively decreases, whereas that of L_2-b increases as $Fe^{3+}/\Sigma Fe$ increases. The energy position of L_2-b changes very weak between the samples, whereas peaks L_3-a and L_2-a shift slightly towards higher energies when $Fe^{3+}/\Sigma Fe$ increases.

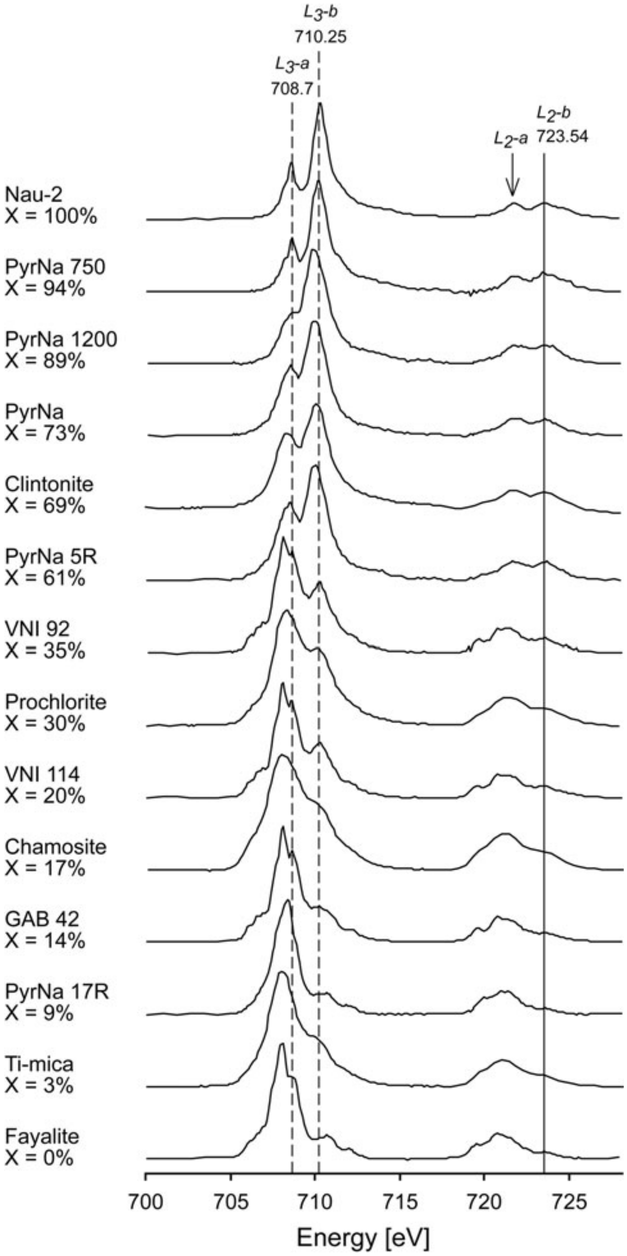

Fig. 2 Representative XANES spectra at the Fe $L_{2,3}$-edges for the reference silicates. The spectra have been normalised to the integral Fe L_3-edge intensity, and some of the spectra have been shifted vertically for clarity (normalised intensity with arbitrary units). The dotted lines represent the energies fixed to determine the Fe^{3+} concentration from the Fe L_3-peaks' intensity ratio. The solid line underlines the position of L_2-b maximum intensity, which is identical for all spectra. X = $Fe^{3+}/\Sigma Fe$ ratios of Table 1

Quantification of $Fe^{3+}/\Sigma Fe$ from XANES Fe $L_{2,3}$-edge intensity ratios

As documented in Fig. 2, the main variations in the XANES spectra of reference samples with varying $Fe^{3+}/\Sigma Fe$ ratios involve the L_3-b/L_3-a intensity ratio. More precisely, the L_3-b/L_3-a intensity ratio is linearly correlated

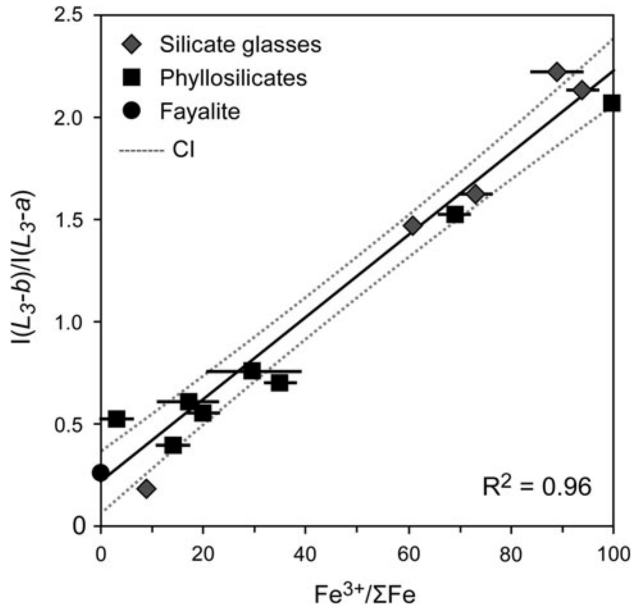

Fig. 3 L_3-edge intensity ratio *I(L_3-b)/I(L_3-a)* from XANES spectra versus ferric iron concentration $Fe^{3+}/\Sigma Fe$ quantified by independent methods for the selected silicates. *CI* confidence interval (95 %)

with $Fe^{3+}/\Sigma Fe$ ratio with only a little scatter ($R^2 = 0.96$) for both the phyllosilicates and silicate glasses (Fig. 3). The correlation is described by Eq. (2):

$$\frac{Fe^{3+}}{\sum Fe} = \frac{R_{L_3} - 0.1867}{0.01991} \text{ with } R_{L_3} = \frac{I(L_3 - b)}{I(L_3 - a)} \qquad (2)$$

This approach requires only five XANES images to map $Fe^{3+}/\Sigma Fe$ (see Fig. 4 and below): two images in the pre-edge (needed to apply the "linear background correction" at each pixel of the image), one at 708.7 eV to quantify the L_3-a peak, one at 710.25 eV to quantify the L_3-b peak and one at 718 eV, to remove the edge step of the arctan function. Finally, the ratio of the resulting 708.7 and 710.25 eV images can be used to determine the R_{L3} parameter at each pixel of the image.

This calibration is useful but has some limitations. The L_3 peaks, which are much more intense than the L_2 peaks, are more susceptible to absorption saturation (see Hanhan et al. 2009, where saturation effects are described for Ca 2p edge spectra). This phenomenon occurs when the sample is too thick and/or highly concentrated in Fe implying that few photons are transmitted. This may trigger a nonlinear response of the detection and an artifactual modification of the relative peak heights. The use of a spectral parameter correlated with $Fe^{3+}/\Sigma Fe$ based on the less absorbing L_2-edge may provide in this case an interesting way of circumventing absorption saturation issues encountered with the L_3-edge.

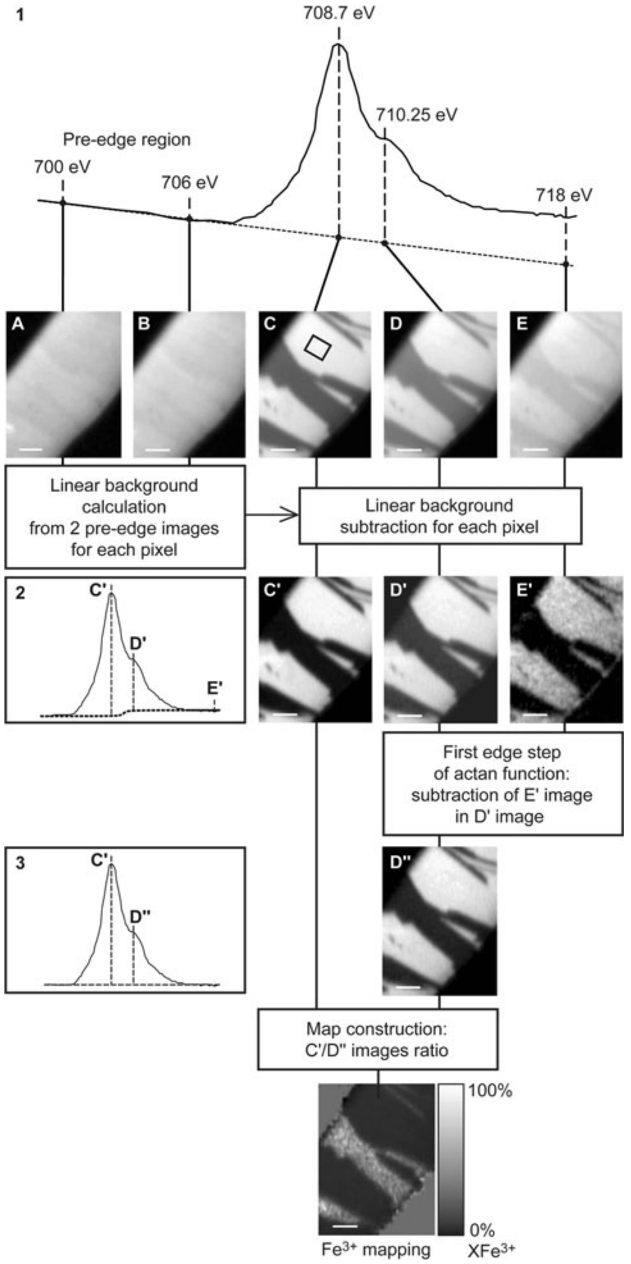

Fig. 4 Determination of the $Fe^{3+}/\Sigma Fe$ ratio from 5 selected energy images: two images in the pre-edge (to apply the "linear background correction" at each pixel of the image), one at 708.7 eV to quantify the L_3-a peak, one at 710.25 eV to quantify the L_3-b peak and one at 718 eV, to remove the edge step of the arctan function. Finally, the ratio of the resulting 708.7 and 710.25 eV images can be used to determine the R_{L3} parameter at each pixel of the image and obtain iron redox mapping. All images are OD images (70 × 90 pixels), where the illite and chlorite are the *dark-* and *light-grey* phases, respectively. As an illustration, spectrum #1 was retrieved from 110 images (i.e., 110 energy points) on a chlorite area (*dark rectangle on image C*); spectrum #2 was obtained after the linear function subtraction from spectrum #1 and spectrum #3, after the actan function subtraction from spectrum #2. Case of FIB foil of Glarus GL07 20 sample

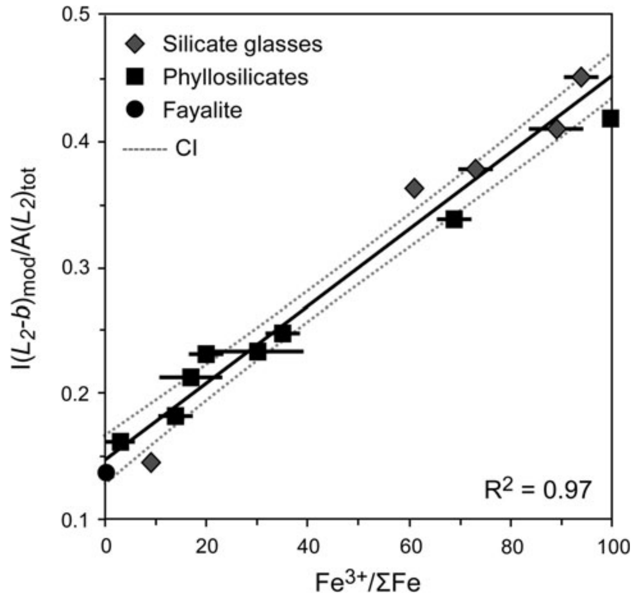

Fig. 5 L_2-edge integral intensity ratio (i.e., integral intensity of maximum L_2-b ± 0.1 eV over total integral intensity (*area*) of L_2-edge) from XANES spectra versus ferric iron concentration $Fe^{3+}/\Sigma Fe$ quantified by independent methods for the reference silicates. *CI* confidence interval (95 %)

Figure 2 shows that an increase in $Fe^{3+}/\Sigma Fe$ is associated with a decrease in the intensity of L_2-a. Figure 5 shows the correlation between $Fe^{3+}/\Sigma Fe$ and R_{L2}, a ratio that reflects the importance of L_2-b relative to the total L_2. Similar to the modified intensity defined by van Aken and Liebscher (2002), the L_2-b contribution is computed as an integration window of 2 eV width centred around the maximum L_2-b intensity; the ratio R_{L2} is calculated from this modified L_2-b intensity and the total integral intensity of L_2-edge. The correlation is high ($R^2 = 0.97$), and is described by Eq. (3):

$$\frac{\mathrm{Fe}^{3+}}{\sum \mathrm{Fe}} = \frac{R_{L_2} - 0.1476}{0.00297} \text{ with } R_{L_2} = \frac{I(L_2 - b)_{\text{mod}}}{A(L_2)_{total}} \qquad (3)$$

This approach requires the acquisition of a complete stack of images (i.e., as many images as energy points are required to obtain a complete spectrum with a given spectral resolution) between 715 and 730 eV, to cover the entire L_2-edge, and to calculate the double arctan function (Eq. (1)). As a consequence, the acquisition time required for this method is longer than for the L_3-b/L_3-a intensity ratio method (e.g., 30–40 min versus 5–10 min for an area of 150 by 150 pixels). However, this second method seems to be more accurate, especially because (1) the calibration data are less scattered (Fig. 5 versus Fig. 3) and (2) the intensity integration improves the signal-to-noise ratio. Several other methods of calibration have been tested, sometimes giving equation with a high correlation (with a R^2 up to 0.95), but the two methods proposed here seem to be a good trade-off between $Fe^{3+}/\Sigma Fe$ estimation accuracy, acquisition time and ease of use.

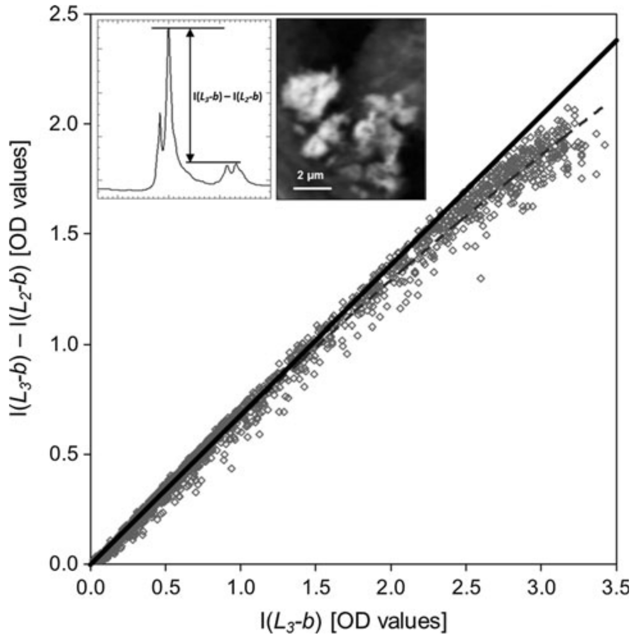

Fig. 6 Difference, pixel by pixel, of intensity detected between the 710.25 and the 723.54 eV images (in which a pre-edge image was not subtracted) versus the intensity of the 710.25 eV image of a Smectite Nau-2 STXM-map (Nau-2, 72 × 88 pixels = 6336 points), that is, the L_3-b – L_2-b intensity difference versus the L_3-b intensity for each pixel. The dashed line was calculated from a quadratic equation. Insets: representative spectra and optical density image (710.25 eV) for Nau-2 sample

Assessment of saturation and beam damage effects

When particles are sufficiently thin, the intensity of each spectral feature changes linearly with thickness. However, Hanhan et al. (2009) showed that in the case of samples that are too thick, one can observe distortions of the Ca 2p spectrum due to a saturation effects. These observations led the authors of that study to set a maximum peak intensity, which should not be exceeded to avoid saturation phenomena.

Similarly, we determined the maximum peak intensity below which the Fe L_{23} spectra are undistorted and vary linearly. For this purpose, a powder of the smectite Nau-2 sample with grains of various sizes was analysed by STXM. Figure 6 plots the difference between the intensities at 710.35 (L_3-b) and 723.54 eV (L_2-b) (corrected from the pre-edge slope) versus the intensity at 710.35 eV (L_3-b, i.e., the peak of maximum intensity for Nau-2, hence the most susceptible to saturation) for each pixel of the stack of images (i.e., a total of 6,336 pixels). The difference between L_3-b and L_2-b intensities increases linearly when L_3-b intensity is lower than ~1.5 OD. Once the L_3-b intensity exceeds 1.5 OD, the L_3-b–L_2-b difference increases more slowly than L_3-b, underlining (1) the

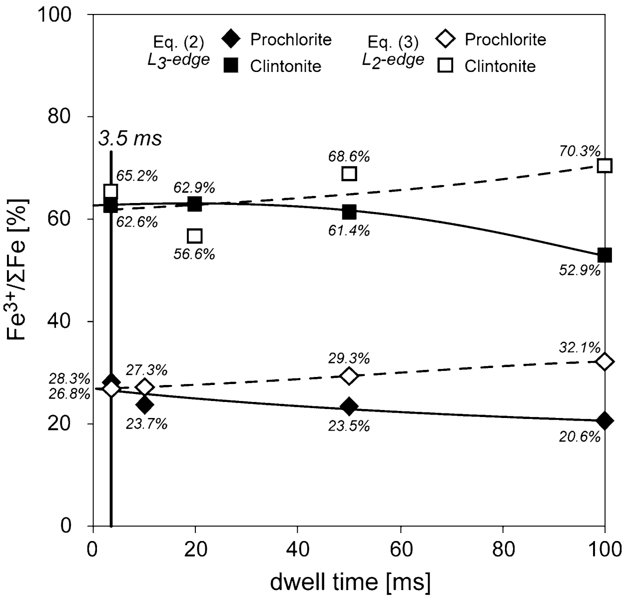

Fig. 7 Beam-induced radiation damage during STXM analyses of chlorite “prochlorite” ($XFe^{3+} = 30$ %) and clintonite ($XFe^{3+} = 69$ %). Evolution of the $Fe^{3+}/\Sigma Fe$ ratios as a function of dwell time, estimated by Eqs. (2) and (3) from XANES spectra. Data were fit by a quadratic function. The beam radiations (*increasing dwell*) involve (1) a decrease in XFe^{3+} calculated from L_3-edge (Eq. 2) and (2) an increase in XFe^{3+} calculated from L_2-edge (Eq. 3). Spectra of reference samples and Glarus samples (see text) were recorded with a dwell time of 1.3-3.5 ms per point and energy: the beam radiation damage is thus negligible with our analytical conditions for data collection

distortion of the spectra for the considered pixels and (2) the faster increase in L_2-b intensity compared to that of L_3-b with increasing sample thickness. All the data presented in this study were therefore collected from areas presenting a L_3 peak intensity lower than 1.5 OD.

The spectrum may be also influenced by the crystal orientation relative to the direction of polarisation of the X-ray beam, a process called linear dichroism. Therefore, several XANES spectra were measured on the same part of a FIB foil after sequential rotation of the linear polarisation (see Benzerara et al. 2011b for details on the procedure). The variation of resulting $Fe^{3+}/\Sigma Fe$ estimates is negligible, showing that sample orientation does not affect the Fe^{3+} quantification.

Beam damage can also potentially alter assessment of the $Fe^{3+}/\Sigma Fe$ ratio. Here, beam damage was evaluated by monitoring spectral changes at the Fe $L_{2,3}$-edge with increasing dwell times from 10 up to 100 ms. Figure 7 shows that $Fe^{3+}/\Sigma Fe$ ratios derived from XANES spectra are only slightly affected by increasing dwell time. In particular, no significant change was observed for typical dwell times used during routine analyses of the samples (i.e., ~1.3 and 3.5 ms per energy- and image-point for ALS and SLS synchrotrons, respectively).

Application to a geological case: chlorites and micas from Glarus (Central Alps, Switzerland)

To go further, we have applied the methods proposed here on micrometre-sized chlorite and mica/illite-like grains sampled in the Glarus area of Switzerland and cut by FIB milling. The temperatures of chlorite formation were calculated from analytical electron microscopy (AEM) chemical analyses, based on the thermometer by Bourdelle et al. (2013b), which does not require $Fe^{3+}/\Sigma Fe$ input, and the thermometer by Inoue et al. (2009), which needs a previous estimation of Fe^{3+} content. The $Fe^{3+}/\Sigma Fe$ ratios were estimated for each FIB foil by XANES from Eqs. (2) and (3). The results are given in Fig. 8 and Table 2.

From images converted to optical density units taken at 708.7 eV, we can easily distinguish Fe-rich and Fe-poor minerals: chlorites appear as light grey and represent the Fe-rich phase, whereas micas are dark, that is, Fe-poor. XANES spectra, acquired along the mica-chlorite contacts show that the $Fe^{3+}/\Sigma Fe$ ratio is higher in illite than in chlorite: the $Fe^{3+}/\Sigma Fe$ ratios estimated by Eq. (3) range from 22.3 to 27.9 % in chlorite, whereas these ratios vary between 30 and 65.5 % in illite-like phase. Equation (2) provides consistent estimations, suggesting that both calibrations are reliable. This analysis shows that K-deficient micas can contain a high proportion of ferric iron (e.g., samples 13 and 20). Despite the relatively high $Fe^{3+}/\Sigma Fe$ ratio in some illite-like crystals, the total Fe^{3+} content remains higher in chlorite.

Figure 8 also shows the variations of $Fe^{3+}/\Sigma Fe$ ratios versus the temperature of formation, which was estimated by chlorite thermometry (Table 2). In this respect, $Fe^{3+}/\Sigma Fe$ ratio increases slightly in chlorites with increasing temperature, whereas this ratio decreases in K-deficient micas. It should be noted that, contrarily to the Bourdelle et al. (2013b) model, some geothermometers based on thermodynamic models for chlorite (e.g., Inoue et al. 2009) require prior determination of the $Fe^{3+}/\Sigma Fe$ ratio. When this value is not known, it is set to zero as the default in these types of models. Interestingly, the comparison of results provided by different thermometers in Table 2 shows that the Inoue and Bourdelle geothermometers yield very different temperature results (differences of up to 76 °C) when $Fe^{3+}/\Sigma Fe$ ratio is not known. In contrast, taking into account the $Fe^{3+}/\Sigma Fe$, the two thermometers provide more similar temperatures estimates (a maximum difference of less than 28 °C, i.e., within the uncertainty of the thermometers), showing the cross-check validity of the $Fe^{3+}/\Sigma Fe$ estimation. A variation of the $Fe^{3+}/\Sigma Fe$ ratio from 0 to ~23 % in chlorites implies a decrease in the temperatures calculated by the Inoue model of 20, 40 and 46 °C depending on the sample.

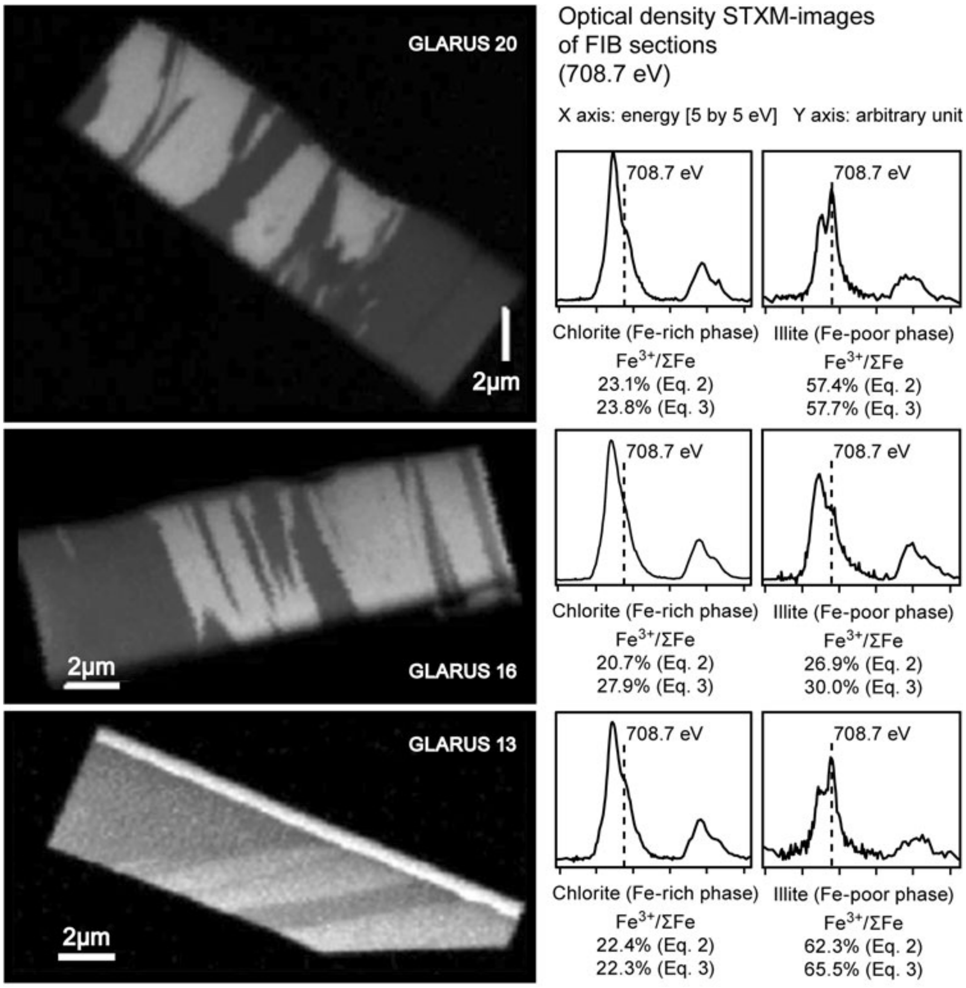

Fig. 8 Scanning transmission X-ray microscopy (STXM) and XANES analysis and $Fe^{3+}/\Sigma Fe$ estimations for FIB foils of Glarus samples (*chlorite and illite*). [*Left*] Optical density images of FIB foils at 708.7 eV. The illite and chlorite are the dark- and light-grey phases, respectively. [*Right*] XANES spectra of areas of interest and calculated Fe^{3+} concentrations associated (*crystals rims*)

Table 2 AEM chemical representative analyses of Glarus chlorites and comparison of thermometers results taking into account $Fe^{3+}/\Sigma Fe$ ratios (Eq. (3)); regarding the scatter of data on Fig. 3, we infer a precision of ±5 % on the $Fe^{3+}/\Sigma Fe$

Chlorite [%wt]	GL07 13	GL07 20	GL07 16
SiO_2	32.70	31.40	31.57
TiO_2	0.07	0.06	0.04
Al_2O_3	26.41	25.56	26.02
FeO	26.63	28.53	25.13
MnO	0.00	0.00	0.00
MgO	13.75	13.97	16.70
CaO	0.06	0.10	0.29
Na_2O	0.00	0.04	0.00
K_2O	0.39	0.35	0.25
$Fe^{3+}/\Sigma Fe$ [%]	22.30	23.80	27.90
T_{BOU} [°C]	135	170	182
$T_{INO\text{-}Fe2+}$ [°C]	165 (+*30*)	236 (+*66*)	258 (+*76*)
$T_{INO\text{-}Fe3+}$ [°C]	145 (+*10*)	196 (+*26*)	210 (+*28*)

Analyses were carried out on crystal rims, along the illite-chlorite contact, according to Bourdelle et al. (2013a). Temperature estimations were performed with Bourdelle et al. (2013b) and Inoue et al. (2009) thermometers, with and without consideration of Fe^{3+}, in accordance with the recommendations made by each authors. Italic values refer to the difference between the temperatures calculated by the Inoue model and the Bourdelle model. Taking into account the $Fe^{3+}/\Sigma Fe$ ratios in the Inoue model allows to obtain similar results to those calculated with the Bourdelle model (which is a pure Fe^{2+} model), that is, with a difference less than 30 °C (equivalent to the uncertainty of each model)

T_{BOU}: temperatures calculated with the Fe^{2+}-pure model of Bourdelle et al. (2013b), considering $Fe_{tot} = Fe^{2+}$. $T_{INO\text{-}Fe2+}$: temperatures calculated with the Inoue et al. (2009) model, considering $Fe_{tot} = Fe^{2+}$. $T_{INO\text{-}Fe3+}$: temperatures calculated with the Inoue et al. (2009) model, using the estimated $Fe^{3+}/\Sigma Fe$

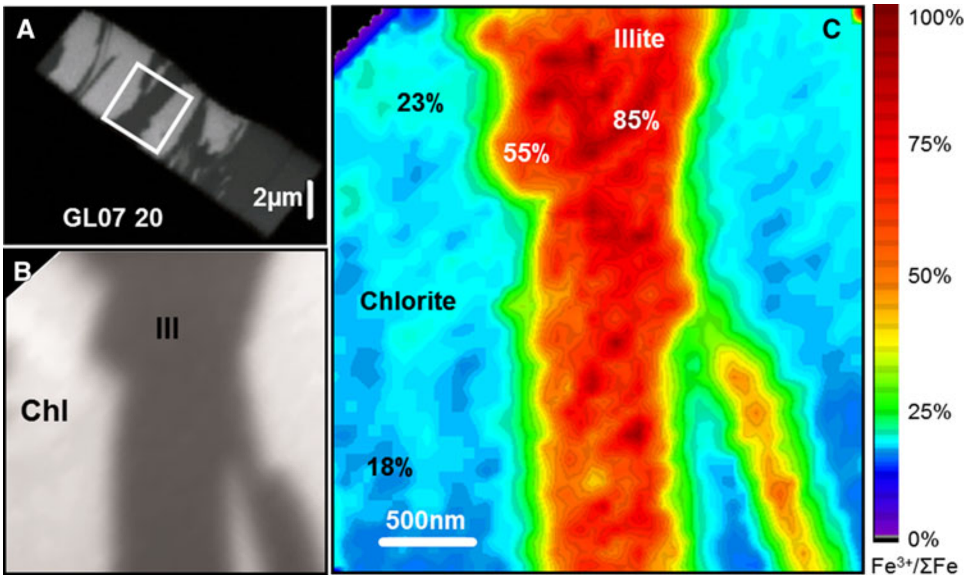

Fig. 9 Quantitative Fe redox nanomapping on FIB foil of Glarus GL07 20 sample. *a* Optical density image at 708.7 eV of Glarus GL07 20 FIB section, where the illite and chlorite are the *dark*- and light-*grey* phases, respectively. *b* Optical density image at 708.7 eV of the area of interest. *c* iron redox mapping, calculated from the 708.7 to 710.25 eV images ratio coupled with Eq. (2). The illite-chlorite contacts were analysed by AEM to check that they are approximately perpendicular to the FIB foil surface, that is, there is only a small overlap between the two minerals at their contact. The spatial averaging effect of the X-ray beam over the pixel size (i.e., 88 nm) sets the limit of the minimum distance over which illite-chlorite contacts can be discriminated. Beyond this distance, the intracrystalline variation of $Fe^{3+}/\Sigma Fe$ ratio in the illite-like phase can be interpreted as an authentic zonation, from 55 to 85 % in several crystal core clusters

Figure 9 displays an example of $Fe^{3+}/\Sigma Fe$ mapping at the nanometre-scale derived from images at 706, 708.7, 710.25 and 718 eV using Eq. (2) (see Fig. 4). The analysis was carried out on the Glarus GL07 20 FIB foil. The scanned area measures 3.3 × 3.5 micrometres with a pixel size of 88 × 88 nm. The analysis of the illite-chlorite contacts by AEM showed that they are approximately perpendicular to the FIB foil surface, that is, there is only a little overlap between the two minerals at their contact. The spatial averaging effect of the X-ray beam over the pixel size (i.e., 88 nm) sets the limit of the minimum distance over which illite-chlorite contacts can be discriminated. Beyond this distance, the intracrystalline variation of the $Fe^{3+}/\Sigma Fe$ ratio in the illite-like phase can be interpreted as an authentic zonation, from ~55 % in crystal rims (conforming to the spectra presented in Fig. 8) to ~85 % in several crystal core clusters. In the same way, the $Fe^{3+}/\Sigma Fe$ ratio distribution draws a subtle zonation in the chlorite, with a $Fe^{3+}/\Sigma Fe$ ratio ranging from 18 to ~23 % on the crystal rim, in accordance with the spectra shown in Fig. 8. Such variations of the $Fe^{3+}/\Sigma Fe$ ratio within the crystals are equivalent to several degrees or tens of degrees in the temperature estimation, especially when this variation is associated with a variation in composition. One can expect that this zonation is a crucial issue in application of geothermometers (de Andrade et al. 2006; Bourdelle et al. 2013a), and the redox gap between illite and chlorite raises the issue of the crystallisation processes.

In summary, the STXM-based XANES study of FIB foils from the Glarus, Switzerland samples enables (1) estimation of the $Fe^{3+}/\Sigma Fe$ ratio in each phase and (2) establishment of iron redox mapping with high spatial resolution.

Conclusion

In this study, we have demonstrated the reliability of two methods that allow quantitative determination of $Fe^{3+}/\Sigma Fe$ ratios in silicate phases using STXM coupled with XANES spectroscopy at the Fe $L_{2,3}$-edges. These approaches are similar to those proposed by van Aken and Liebscher (2002) for EELS measurements but are here calibrated for STXM. The two calibrations are based on reference samples with variable but known $Fe^{3+}/\Sigma Fe$ ratios, which were prepared as powders or as FIB foils. We tested these calibrations on three FIB foils extracted from field samples of phyllosilicates (Glarus, Switzerland chlorite and illite samples from metapelites), demonstrating the potential of these methods for quantifying $Fe^{3+}/\Sigma Fe$ ratios at the sub-micrometre scale. This approach will allow more quantitative mineralogical or geomicrobiological studies requiring estimation of the iron redox state at the nanoscale for terrestrial or extraterrestrial Fe-rich samples.

Acknowledgments We are most grateful to the Lawrence Berkeley National Lab and especially to Tolek Tyliszczak for his scientific support, and the Paul Scherrer Institute, Swiss Light Source. We would like to thank the materials characterisation department of IFP Energies nouvelles-Lyon and the laboratory of CP2M-Université Aix-Marseille, for technical advice. Thanks are also extended to Nicolas Menguy for his scientific help and to Christian Chopin (ENS, Paris), Daniel Beaufort (IC2MP, Poitiers), Patricia Patrier (IC2MP, Poitiers) and the Muséum National d'Histoire Naturelle. This study was supported by a grant from the Simone and Cino del Duca Foundation.

References

Bajt S, Sutton SR, Delaney JS (1994) X-ray microprobe analysis of iron oxidation-states in silicates and oxides using X-ray-absorption near-edge structure (XANES). Geochim Cosmochim Ac 58(23):5209–5214

Beaufort D, Patrier P, Meunier A, Ottaviani MM (1992) Chemical variations in assemblages including epidote and/or chlorite in the fossil hydrothermal system of Saint Martin (Lesser Antilles). J Volcanol Geoth Res 51:95–114

Benzerara K, Miot J, Morin G, Ona-Nguema G, Skouri-Panet F, Ferard C (2011a) Significance, mechanisms and environmental implications of microbial biomineralization. C R Geosci 343(2–3):160–167

Benzerara K, Menguy N, Obst M, Stolarski J, Mazur M, Tylisczak T, Brown GE Jr, Meibom A (2011b) Study of the crystallographic architecture of corals at the nanoscale by scanning transmission X-ray microscopy and transmission electron microscopy. Ultramicroscopy 111(8):1268–1275

Bernard S, Benzerara K, Beyssac O, Brown GE Jr (2010) Multiscale characterization of pyritized plant tissues in blueschist facies metamorphic rocks. Geochim Cosmochim Ac 74(17):5054–5068

Berry AJ, O'Neill HS, Jayasuriya KD, Campbell SJ, Foran GJ (2003) XANES calibrations for the oxidation state of iron in a silicate glass 88(7):967–977

Berry AJ, Yaxley GM, Woodland AB, Foran GJ (2010) A XANES calibration for determining the oxidation state of iron in mantle garnet. Chem Geol 278(1–2):31–37

Bluhm H, Andersson K, Araki T, Benzerara K, Brown JGE, Dynes JJ, Ghosal S, Gilles MK, Hansen HC, Hemminger JC, Hitchcock AP, Ketteler G, Kilcoyne ALD, Kneedler E, Lawrence JR, Leppard GG, Majzlam J, Mun BS, Myneni SCB, Nilsson A, Ogasawara H, Ogletree DF, Pecher K, Salmeron M, Shuh DK, Tonner B, Tyliszczak T, Warwick T, Yoon TH (2006) Soft Xray microscopy and spectroscopy at the molecular environmental science beamline at the advanced light source. J Electron Spectrosc 150:86–104

Bolfan-Casanova N, Munoz M, McCammon C, Deloule E, Ferot A, Demouchy S, France L, Andrault D, Pascarelli S (2012) Ferric iron and water incorporation in wadsleyite under hydrous and oxidizing conditions: a XANES, Mossbauer, and SIMS study. Am Mineral 97(8–9):1483–1493

Boulard E, Menguy N, Auzende AL, Benzerara K, Bureau H, Antonangeli D, Corgne A, Morard G, Siebert J, Perrillat JP, Guyot F, Fiquet G (2012) Experimental investigation of the stability of Fe-rich carbonates in the lower mantle. J Geophys Res-Solid Earth 117(B2)

Bourdelle F, Parra T, Beyssac O, Chopin C, Moreau F (2012) Ultrathin section preparation of phyllosilicates by focused ion beam milling for quantitative analysis by TEM-EDX. Appl Clay Sci 59–60:121–130

Bourdelle F, Parra T, Beyssac O, Chopin C, Vidal O (2013a) Clay minerals as geo-thermometer: a comparative study based on high spatial resolution analyses of illite and chlorite in Gulf Coast sandstones (Texas, USA). Am Mineral 98(5–6):914–926

Bourdelle F, Parra T, Chopin C, Beyssac O (2013b) A new chlorite geothermometer for diagenetic to low-grade metamorphic conditions. Contrib Mineral Petr 165:723–735

Brotton SJ, Shapiro R, van der Laan G, Guo J, Glans PA, Ajello JM (2007) Valence state fossils in Proterozoic stromatolites by L-edge X-ray absorption spectroscopy. J Geophys Res-Biogeosci 112:G3

Carlut J, Benzerara K, Horen H, Menguy N, Janots D, Findling N, Addad A, Machouk I (2010) Microscopy study of biologically mediated alteration of natural mid-oceanic ridge basalts and magnetic implications. J Geophys Res-Biogeosci 115(G4)

Chen CT, Idzerda YU, Lin HJ, Smith NV, Meigs G, Chaban E, Ho GH, Pellegrin E, Sette F (1995) Experimental confirmation of the X-ray magnetic circular-dichroism sum-rules for iron and cobalt. Phys Rev Lett 75(1):152–155

Cressey G, Henderson CMB, Vanderlaan G (1993) Use of L-edge X-Ray-absorption spectroscopy to characterize multiple valence states of 3d transition-metals: a new probe for mineralogical and geochemical research. Phys Chem Miner 20(2):111–119

Crocombette JP, Pollak M, Jollet F, Thromat N, Gautiersoyer M (1995) X-Ray-absorption spectroscopy at the Fe L(2,3) threshold in iron-oxides. Phys Rev B 52(5):3143–3150

de Andrade V, Vidal O, Lewin E, O'Brien P, Agard P (2006) Quantification of electron microprobe compositional maps of rock thin sections: an optimized method and examples. J Metamorph Geol 24(7):655–668

de Groot FMF, de Smit E, van Schooneveld MM, Aramburo LR, Weckhuysen BM (2010) In-situ scanning transmission X-ray microscopy of catalytic solids and related nanomaterials. ChemPhysChem 11(5):951–962

de Smit E, Swart I, Creemer JF, Hoveling GH, Gilles MK, Tyliszczak T, Kooyman PJ, Zandbergen HW, Morin C, Weckhuysen BM, de Groot FMF (2008) Nanoscale chemical imaging of a working catalyst by scanning transmission X-ray microscopy. Nature 456(7219):U222–U239

Fialin M, Bézos A, Wagner C, Magnien V, Humler E (2004) Quantitative electron microprobe analysis of $Fe^{3+}/\Sigma Fe$: basic concepts and experimental protocol for glasses. Am Mineral 89(4):654–662

Garvie LA, Zega TJ, Rez P, Buseck PR (2004) Nanometer-scale measurements of $Fe^{3+}/\Sigma Fe$ by electron energy-loss spectroscopy: a cautionary note. Am Mineral 89(11–12):1610–1616

Hanhan S, Smith AM, Obst M, Hitchcock AP (2009) Optimization of analysis of soft X-ray spectromicroscopy at the Ca 2p edge. J Electron Spectrosc 173(1):44–49

Heaney PJ, Vicenzi EP, Giannuzzi LA, Livi KJT (2001) Focused ion beam milling: a method of site-specific sample extraction for microanalysis of Earth and planetary materials. Am Mineral 86(9):1094–1099

Heijboer WM, Battiston AA, Knop-Gericke A, Havecker M, Mayer R, Bluhm H, Schlogl R, Weckhuysen BM, Koningsberger DC, de Groot FMF (2003) In-situ soft X-ray absorption of over-exchanged Fe/ZSM5. J Phys Chem B 107(47):13069–13075

Hitchcock AP (2012) aXis 2000 analysis of X-ray images and spectra. McMaster University, Hamilton

Inoue A, Meunier A, Patrier-Mas P, Rigault C, Beaufort D, Vieillard P (2009) Application of chemical geothermometry to low temperature trioctahedral chlorites. Clay Clay Miner 57(3): 371–382

Joswig W, Amthauer G, Takeuchi Y (1986) Neutron-diffraction and Mössbauer spectroscopic study of clintonite (xanthophyllite). Am Mineral 71:1194–1197

Keeling JL, Raven MD, Gates WP (2000) Geology and characterization of two hydrothermal nontronites from weathered metamorphic rocks at the Uley graphite mine South Australia. Clay Clay Miner 48(5):537–548

Lahfid A, Beyssac O, Deville E, Negro F, Chopin C, Goffe B (2010) Evolution of the Raman spectrum of carbonaceous material in low-grade metasediments of the Glarus Alps (Switzerland). Terra Nova 22(5):354–360

Lam KP, Hitchcock AP, Obst M, Lawrence JR, Swerhone GDW, Leppard GG, Tyliszczak T, Karunakaran C, Wang J, Kaznatcheev K, Bazylinski DA, Lins U (2010) Characterizing magnetism of individual magnetosomes by X-ray magnetic circular dichroism in a scanning transmission X-ray microscope. Chem Geol 270(1–4):110–116

Lauterbach S, McCammon CA, van Aken P, Langenhorst F, Seifert F (2000) Mossbauer and ELNES spectroscopy of (Mg, Fe)(Si, Al)O3 perovskite: a highly oxidised component of the lower mantle. Contrib Mineral Petr 138(1):17–26

Magnien V, Neuville DR, Cormier L, Mysen BO, Briois V, Belin S, Pinet O, Richet P (2004) Kinetics of iron oxidation in silicate melts: a preliminary XANES study. Chem Geol 213(1–3): 253–263

Miot J, Benzerara K, Morin G, Kappler A, Bernard S, Obst M, Ferard C, Skouri-Panet F, Guigner JM, Posth N, Galvez M, Brown GE Jr, Guyot F (2009) Iron biomineralization by anaerobic neutrophilic iron-oxidizing bacteria. Geochim Cosmochim Ac 73(3):696–711

Miot J, Maclellan K, Benzerara K, Boisset N (2011) Preservation of protein globules and peptidoglycan in the mineralized cell wall of nitrate-reducing, iron (II)-oxidizing bacteria: a cryo-electron microscopy study. Geobiology 9(6):459–470

Munoz M, De Andrade V, Vidal O, Lewin E, Pascarelli S, Susini J (2006) Redox and speciation micromapping using dispersive X-ray absorption spectroscopy: Application to iron chlorite mineral of a metamorphic rock thin section. Geochem Geophys Geosyst 7(11)

Raabe, J, Tzvetkov, G, Flechsig, U, Böge, M, Jaggi, A, Sarafimov, B, Vernooij, MGC, Huthwelker, T, Ade, H, Kilcoyne, D, Tyliszczak, T, Fink, RH Quitmann, C (2008) PolLux: A new facility for soft X-ray spectromicroscopy at the Swiss Light Source. Rev Sci Instrum 79(11)

Raeburn SP, Ilton ES, Veblen DR (1997a) Quantitative determination of the oxidation state of iron in biotite using X-ray photoelectron spectroscopy: I Calibration. Geochim Cosmochim Ac 61(21):4519–4530

Raeburn SP, Ilton ES, Veblen DR (1997b) Quantitative determination of the oxidation state of iron in biotite using X-ray photoelectron spectroscopy: II In situ analyses. Geochim Cosmochim Ac 61(21):4531–4537

Rigault C (2010) Cristallochimie de Fer dans les chlorites de basse température : implications pour la géothermométrie et la détermination des paléoconditions redox dans les gisements d'Uranium. University of Poitiers, Poitiers

Schingaro E, Scordari F, Mesto E, Brigatti MF, Pedrazzi G (2005) Cation-site partitioning in Ti-rich micas from Black Hill (Australia): a multi-technical approach. Clay Clay Miner 53(2):179–189

Schmid R, Wilke M, Oberhänsli R, Janssens K, Falkenberg G, Franz L, Gaab A (2003) Micro-XANES determination of ferric iron and its application in thermobarometry. Lithos 70(3–4):381–392

Stagno V, Ojwang DO, McCammon CA, Frost DJ (2013) The oxidation state of the mantle and the extraction of carbon from Earth's interior. Nature 493:84–88

van Aken PA, Liebscher B (2002) Quantification of ferrous/ferric ratios in minerals: new evaluation schemes of Fe L-23 electron energy-loss near-edge spectra. Phys Chem Miner 29(3):188–200

van der Laan G, Kirkman IW (1992) The 2p Absorption-Spectra of 3d transition-metal compounds in tetrahedral and octahedral symmetry. J Phys-Condes Matter 4(16):4189–4204

Wasinger EC, de Groot FMF, Hedman B, Hodgson KO, Solomon EI (2003) L-edge X-ray absorption spectroscopy of non-heme iron sites: experimental determination of differential orbital covalency. J Am Chem Soc 125(42):12894–12906

Waychunas GA, Apted MJ, Brown GE Jr (1983) X-ray K-edge absorption spectra of Fe minerals and model compounds: near-edge structure. Phy Chem Min 10(1):1–9

Wilke M, Farges F, Petit PE, Brown GE Jr, Martin F (2001) Oxidation state and coordination of Fe in minerals: an FeK-XANES spectroscopic study. Am Mineral 86(5–6):714–730

Wilke M, Hahn O, Woodland AB, Rickers K (2009) The oxidation state of iron determined by Fe K-edge XANES-application to iron gall ink in historical manuscripts. J Anal Atom Spectrom 24(10):1364–1372